Three dimensional studies of particle failure in silicon based composite electrodes for lithium ion batteries

Joseph Gonzalez [a], Ke Sun [b], Meng Huang [b], John Lambros [a, *], Shen Dillon [b], Ioannis Chasiotis [a]

[a] Department of Aerospace Engineering, University of Illinois at Urbana-Champaign, USA
[b] Department of Material Science and Engineering, University of Illinois at Urbana-Champaign, USA

HIGHLIGHTS

- Visualized 3D Si particle evolution after varying lithiation levels.
- Quantified Si particle volume expansions up to 290% after 100% lithiation.
- Si particle crack initiation occurs on external surface propagating inward.
- X-ray attenuation of Si decreases with increasing lithiation implying phase changes.
- Less than 5% of total Si particles in electrode never experience full lithiation.

ARTICLE INFO

ABSTRACT

Silicon based composite electrodes for lithium ion batteries are of significant interest because of their potential to be high capacity alternatives to the commonly used graphitic carbon anodes. A drawback to their use, however, is the Si particle debonding and fracture that occurs as a result of the volumetric expansion by the lithium host particles upon lithiation of the anode electrode. We use X-ray micro computed tomography to visualize the evolution of the internal microstructure of a silicon-based electrode before and after four lithiation steps during the first half cycle of the cell. We develop a novel threshold edge detect method to perform 3D volumetric measurements of silicon particle expansion. According to our results, 100% lithiation of the composite anode resulted in up to 290% volume expansion of individual Si particles. Furthermore, the global and localized image intensity histogram profiles from 3D data were used to analyze the silicon particle X-ray attenuation effects as a function of lithiation: a decreasing attenuation with lithiation and the propagation of the reaction front through a core−shell process between the original state and 25% lithiation of the silicon-based electrode have been observed.

© 2014 Elsevier B.V. All rights reserved.

1. Introduction

Since its commercialization in the early 1990s, the lithium ion battery (LIB) has revolutionized energy storage for systems requiring capabilities such as high energy, power, and cyclability [16,19]. However, current LIBs based on traditional transition metal oxide cathodes and graphite anodes are being pushed to their limits. To achieve the next generation LIBs, advanced chemistries with higher volumetric and gravimetric energy densities need to be developed, such as Si and Sn-based anode materials [10,23]. Si and Sn are known to deliver much higher gravimetric capacity than graphite when reacted with lithium because both of them can be theoretically lithiated to $Li_{4.4}Si$ or $Li_{4.4}Sn$. However, when fully lithiated Si and Sn undergo significant volume expansion, as high as ~300% for Si, which leads to pulverization of the electrode particles and eventual loss of functionality [2].

Many strategies have been proposed to mitigate the consequences of this large volume expansion including: using a Si composite instead of pure Si [1,13], using nanoscale Si particles [4,12], and applying incomplete charge and discharge cycles [14]. Among these different strategies, it has been shown that nanoscale Si can completely eliminate cracking while fully taking advantage of the material's high gravimetric capacity. However, because of the high reactivity of Si nanoparticles and nanowires, it is difficult to scale up and mass-produce such configurations. Additionally, the

large surface of Si nanoparticles promotes the formation of a significant solid electrolyte interface (SEI), and reduces the effective volumetric capacity of the anode. Therefore, the process of mechanical failure of micron size Si particles still has to be fully understood in order to be used as a viable anodic electrode material [21].

Various works have been undertaken in the recent years to numerically simulate the evolution of mechanical stresses and understand the mechanical failure of individual Si particles during the lithiation–delithiation process [6,7,26,27]. Due to the intricate relationships between the chemical reaction and mechanical deformation, different approximations and assumptions have been introduced in simulation efforts leading to opposing predictions. Ref. [27] found crack propagation beginning from the surface of the Si particle based on an assumption of no reaction boundaries and allowing only elastic deformation to accommodate strain. The work of Ref. [6] concluded a different effect wherein crack propagation occurs in the opposite direction, *i.e.*, crack formation begins in the interior of a particle, based on the assumption that plastic flow is the only deformation allowed and phase boundary movement is the rate limiting step of the lithiation process. In actuality both mechanisms may occur and may be influenced, especially in the case of highly heterogeneous composite electrodes, by particle shape, size, and distribution, making the problem even more complex than the models discussed above. Therefore, to shed light on these issues, it is desirable to observe the morphological change of a distribution of active particles using three dimensional (3D) high-resolution imaging techniques which can provide insight into volumetric data compared to two dimensional (2D) measurements [2,5].

With recent advancements in 3D imaging, several studies have resulted in quantification of the microstructural evolution of composite structures via X-ray micro computed tomography (microCT) and transmission X-ray microscopy [5,17,22]. Specifically for battery electrodes, which consist of Li$^+$ host particles embedded in a conductive matrix of PVDF and carbon black, such imaging can provide information on percolation effects, phase tortuosity, and particle connectivity. Laboratory and synchrotron X-ray CT have been used to resolve such structures in 3D using active particles such as graphite, Sn, and SnO [8,9,11,17,18,20,24,25]. For example Ref. [9] visualized SnO active particles during the reduction and oxidation processes by using a high-resolution synchrotron radiation X-ray tomographic microscopy (SRXTM). In a different work by Ref. [8]; SRXTM was applied to transition metal oxide-based porous electrodes to obtain 3D reconstructions of the electrode microstructure and quantify properties such as porosity, tortuosity, and particle fracture.

In the present work, we employ X-ray microCT to visualize the microstructural evolution of Si-based electrodes before and after lithiation using a custom designed LIB cell. Through *ex situ* imaging of the composite electrode after different stages of electrochemical testing, we obtained microstructural visualizations and measurements of the particle volume expansion, which provided understanding of the influence of the internal microstructure and its relation to electrochemical performance, thus establishing 3D structure–property relations.

2. Experimental procedures

2.1. Assembly of custom battery cell

Si powder (22% vol., Noah Technologies Corp., 140 mesh), sodium carboxymethyl cellulose (Sigma Aldrich) and Super P carbon (TIMCAL) with a combined volume ratio of (78% vol.) were mixed with distilled water in a mortar with a pestle to form a viscous slurry to fabricate Si composite electrodes compatible with X-ray

tomography. The slurry was further homogenized with a planetary mixer (Thinky). Subsequently, 0.1 ml of slurry was cast and sandwiched between two glass slides with a spacer height of 2 mm. This slurry was heated in vacuum at 80 °C for 48 h to fully evaporate the excess water. The completed composite electrode was diced into smaller pieces (~3.4 mm^3 in volume, 1.5 mm each side of cube) with a razor blade. Each piece was weighed by a digital balance, and the amount of active material, Si particles, was determined from the original mass ratio. Based on this measurement, the current applied during galvanostatic discharge of the LIB cell was calculated. In this study, we use a custom electrode size (~2 mm height) to allow visualization of microstructural changes and to quantify Li$^+$ diffusion along a composite electrode. The relatively large Si particles were selected based on our objectives to analyze the particle evolution and fracture as a function of lithiation coupled with recent renewed interest in developing strategies to utilize micron scale Si particles [21].

A custom designed X-ray transparent, functional, and self-contained LIB cell was assembled and the schematic is shown in Fig. 1. The inner diameter of the transparent tube and the diameter of stainless steel (SS) rods, used as current collectors, were 2 mm. A small copper tube with a thickness slightly smaller than 2 mm served as the current collector for the composite electrode. A spring was placed between the copper tube and the stainless steel rod to ensure electrical contact between the electrode piece and the copper current collector. During assembly, a composite Si electrode was placed on the copper tube and the transparent housing tube was filled with liquid electrolyte (1 M LiClO$_4$ in ethylene carbonate:dimethyl carbonate (1:1 in volume)). A small piece of filter paper (Whatman) and a small strip of lithium were then introduced to act as separator and lithium electrode, respectively. The cell was sealed off at each end of the tube with Torr Seal to prevent leaking. Each packaged LIB cell was left for 24 h in a glove box to ensure the epoxy was fully cured.

A four-step galvanostatic discharge of the LIB cell was gradually applied to lithiate the Si particles in the anodic electrode by increments of 25% of the theoretical lithiation capacity until complete theoretical lithiation. Based on the estimated amount of active Si particles, a C/80 rate was used for the first two increments (up to 50% lithium intercalated), followed by C/160 for the last two
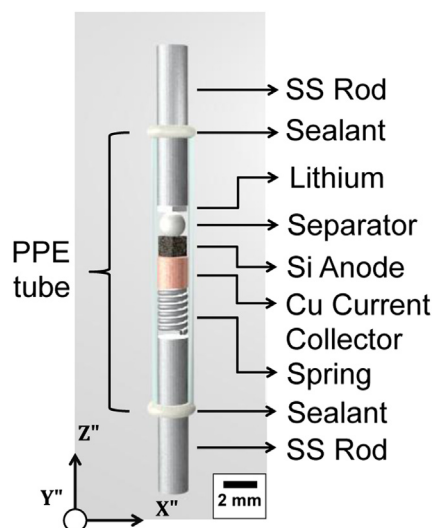

Fig. 1. Custom designed battery cell showing all components of a Li-ion battery. During battery discharge, lithium ions travel from cathode, lithium, through the separator and electrolyte to the anode composed of Si particles. The white material at each side of the LIB cell is Torr Seal, an epoxy to seal and prevent leaking.

increments (until 100% lithiation). Such slow rates were necessary because of the relatively thick electrodes and large Si particles.

2.2. X-ray microtomography process

X-ray tomography via Xradia MicroXCT-400 was conducted on the sample in the original state and after each increment of lithiation. The X-ray MicroCT scan settings, shown in Table 1, were kept consistent for all five (initial and four lithiated) *ex situ* LIB cell scans. Additionally, 4 images per angle increment were averaged to minimize imaging noise. The resultant resolution was 1.89 μm/pixel, or μm/voxel, *i.e.*, voxels are isotropic in size, making the spatial units universal in all three orthogonal directions. The entire 3D volumetric data for each LIB scan consisted of over 800 million voxels and required a scan time of ~90 min. The first scan of the original state of the Si electrode is denoted as 0% lithiation.

In addition to visual observations, the volume expansion of individual Si particles as a function of lithiation was measured. Six Si particles were selected for this purpose near the center of the electrode at various heights (z-axis, see Fig. 1 for coordinates) along the electrode. A thresholding technique was used to measure the particle volume at each of the five scanned states. The particle edge intensity threshold value was determined automatically based on Otsu's threshold method [15] creating a localized threshold value for each region. Contour lines were then used to outline the edges of the particle for each slice enclosing areas used for volumetric computation. Each image slice represented 1 voxel in height (z-direction) enabling the volumetric calculation in units of μm^3. The mean particle intensity was computed from the binary image by locating which coordinates (x, y, z) represented a particle and finding these same locations in the original dataset. The voxels' gray scale values from the raw data were summed and averaged giving particle intensity evolution as a function of lithiation.

3. Results and discussion

The LIB cell was subjected to a galvanostatic discharge in steps until the theoretical capacity was reached. The first half cycle discharge curve is shown in Fig. 2 with each 25% lithiation step denoted by a vertical dashed line. The initial open circuit voltage of the LIB cell was 2.26 V which is marked within the figure. The open circuit voltages at the beginning of every other discharge step are also shown. Following the first discharge step until 25% lithiation, the voltage dropped to 0.03 V. At this point, the LIB cell was disconnected, scanned *ex situ*, and then set up for discharge step 2. In between the X-ray microCT scans, a slight increase in voltage was measured resulting from the LIB cell relaxing toward equilibrium potential while no current was applied. At the beginning of step 2, the measured open circuit voltage was 0.23 V, an increase of 0.2 V. The LIB cell was then discharged further until 50% of the maximum Li intercalated for step 2. The remaining steps were carried out in the same way and the final voltage of the LIB was 0.01 V.

3.1. Global microstructural evolution

As mentioned previously, the Si-based electrode was scanned at 0, 25, 50, 75, and 100% of the theoretical lithiation. In each case, 984
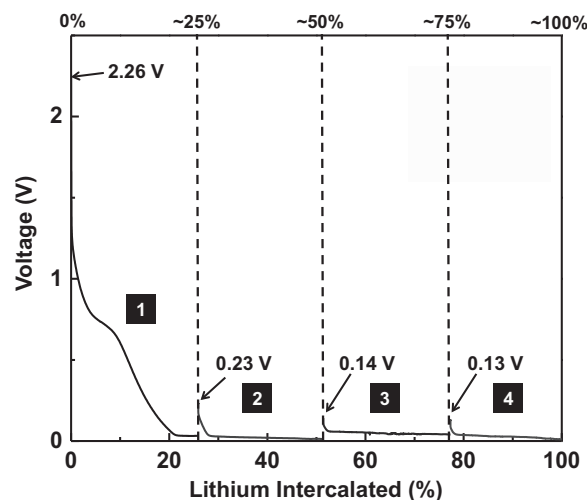

Fig. 2. Galvanostatic discharge of the LIB cell in a series of 4 steps with increments of 25% theoretical lithiation. For steps 1 and 2, a C/80 rate was used, while steps 3 and 4 used a C/160 rate. Following each step, an X-ray microCT scan was taken.

2D images (slices in the vertical direction) were extracted, representing 1860 μm in height and a circular field of view of 1810 μm in diameter. In Fig. 3A–E, the same location in the electrode, 544 μm from the top, is shown as a function of lithium content (slice and particle heights are all referenced from the top of the electrode where is touching the separator, as shown in Fig. 1). The Si particles in Fig. 3A are the *white* irregularly shaped areas and the dark area surrounding them correspond to the porous matrix containing CMC binder, carbon black, and electrolyte. The four regions outlined in each 2D slice, R1, R2, R3, and R4, assist the reader in focusing on areas of particle evolution.

For 0% lithiation (Fig. 3A), all Si particles exhibited a bright intensity with no visible cracking. After 25% lithiation (Fig. 3B), one particle in R1 has visibly decreased intensity, and another particle in R2 begins to develop cracks (both denoted by arrows), while the rest of the particles appear unaffected. Following 50% of lithium intercalation (Fig. 3C), more Si particles begin to develop cracks and lose intensity around the edges, indicating that more cracking is occurring at the outer surface of the particles. Other particles emerge and some disappear in this slice of the electrode because the volumetric changes occurring in the particles drive local rearrangements within the composite electrode. The Si particle in R2 denoted with an arrow experiences crack growth at multiple locations, indicating crack initiation on the external surface and propagation across the particle, similar to the predictions of Ref. [27]. In R4, a large Si particle experiences significant cracking and an increase in the overall cross-sectional area, and consequently its volume. At 75% lithiation (Fig. 3D), the regions of interest begin to clearly expand, and almost all individual Si particles crack and darken considerably, namely undergoing a significant density change. However, a single particle near the top of R1 (denoted by the arrow) remains brighter than the rest and contains only one edge crack, indicating that, although globally the lithiation level is at 75%, this particle was considerably less lithiated. Upon 100% lithiation (Fig. 3E), virtually all particles, except for the one mentioned above, are completely fragmented. At this point it is difficult to distinguish which fragment belonged to each parent Si particle. The drastic particle density change at 100% lithiation is evidenced by the fact that the particles now have an X-ray attenuation coefficient similar to that of the matrix. Essentially all particles in this slice, and similarly in the other slices, have undergone significant volumetric expansion and eventual fragmentation

Table 1
Xradia MicroXCT-400 settings used for Si-based electrode in Li$^+$ battery cell.

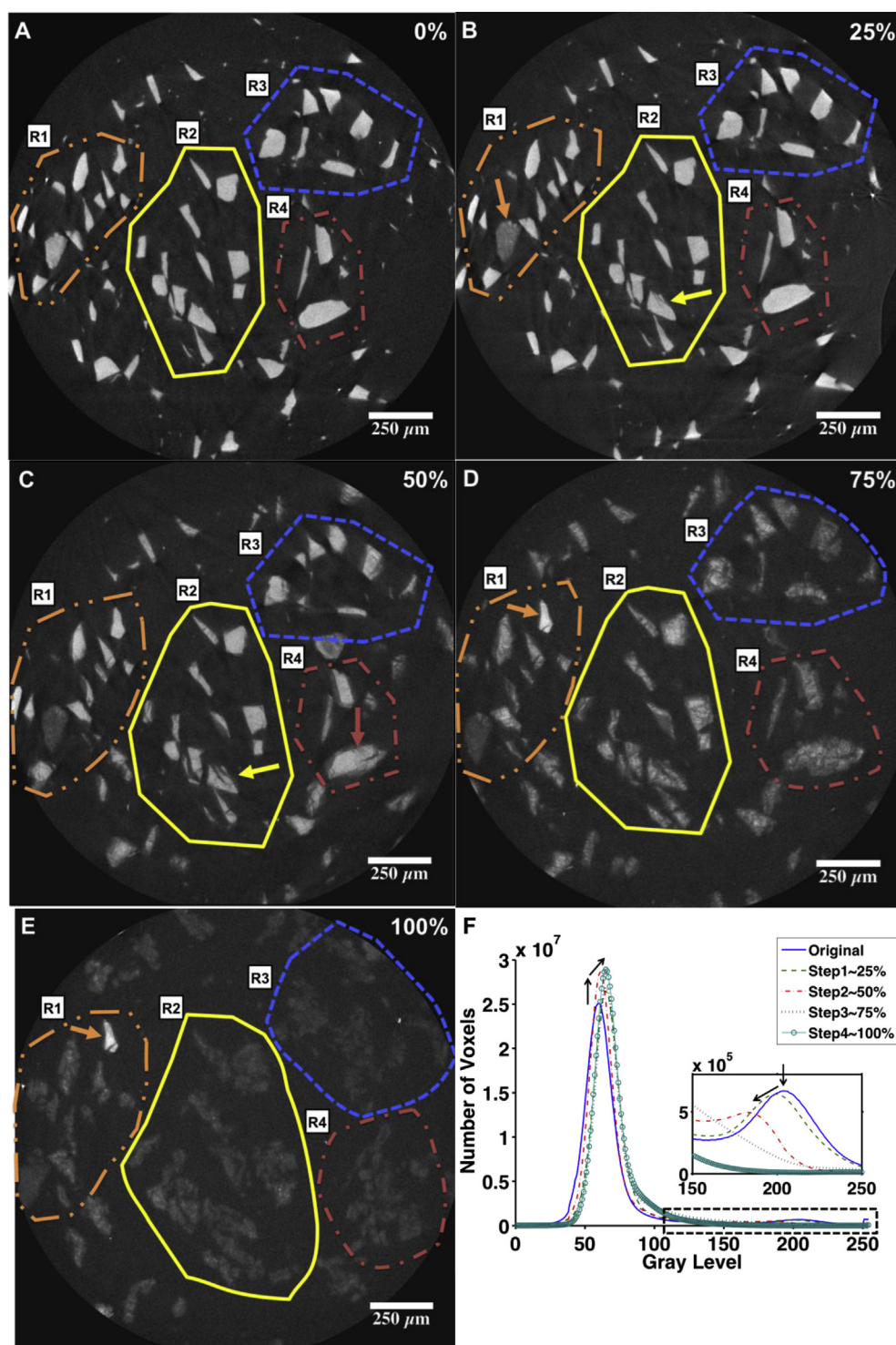| Energy (KeV)	Power (W)	Exposure (s)	Detector-sample distance (mm)	Source-sample distance (mm)	Resolution (μm/pixel)
40	8	3	8.85	25	1.89

Fig. 3. Progression of 2D slices after each lithiation step at a location of 544 μm from the top of the electrode. The bright areas in the 2D slices represent Si particles, which are areas of high X-ray attenuation. The progression of 2D slices from the X-ray microCT scans are shown as follows: (A) the original state, (B) 25% lithiation, (C) 50% lithiation, (D) 75% lithiation, and (E) 100% lithiation. In each 2D slice, there are four regions marked, R1, R2, R3, and R4 to compare the different areas as the amount of lithiation increases. The global histogram is shown (F) for each X-ray microCT scan of 0%, 25%, 50%, 75%, and 100% lithiation showing a decrease in the rightmost peak, defining Si particles, as lithiation increases.

leading to density changes. In addition to the observation of crack occurrence at the surface of the Si particles, the behavior of the particles suggests shear fracture progressing through the interior. The irregular shape and sizes of the Si particles promote this type of anisotropic ductile-type fracture. However, there were Si particles with delayed or no lithiation representing less than 5% of the total, and they consistently appear in all electrodes tested. The cause of

this delayed lithiation may stem from ineffective electrical contact between the Si particle and the matrix, or from shielding by neighboring particles which eliminate the Li$^+$ flux into that specific region.

The images in Fig. 3A–E suggest a correlation between particle damage and image intensity. The global, *i.e.*, over the entire scanned image, gray scale intensity distribution for each X-ray microCT scan

at 0%, 25%, 50%, 75%, and 100% lithiation is shown in Fig. 3F. According to Ref. [3]; each CT Image consists of gray scale intensity values representing the X-ray attenuation of the corresponding voxel, which, in turn, depends on the X-ray attenuation coefficient. For CT scanners operating at relatively high X-ray energies, the attenuation of the X-ray beam is directly proportional to the density of the material at each voxel. For the original CT images at 0% lithiation, there is a bimodal gray level distribution in which the lower intensity peak at gray level 58 corresponds to the binder/electrolyte phase and the high intensity peak gray level 204 is associated with Si particles. As lithiation progresses, the matrix peak shifts to higher intensity values (slightly brighter) while the Si peak shifts toward lower intensity values (darker). At 75% lithiation, the peak corresponding to the Si particles' intensity almost completely merges with the background. This will be further discussed in the context of individual particles in the next section.

Analyzing all particles within the 2D dataset after 50% lithiation, we found that particle size doesn't relate to fracture at this particular length scale in the sense that fracture is seen in all particles visible at this length scale. To determine the length scale of observation in this work, we measured the particle size distribution based on particle volume using 3D thresholding and the particle counter method, with a gray scale intensity threshold of 130. In the sample under discussion here, there were a total of 3572 particles with an average volume of 6.7×10^4 μm^3. The particle distribution was specified with volume rather than particle size because the Si particles are of an irregular platelet-like shape. The volumetric distribution of the Si particles is shown in Fig. 4 where the Si particle count is plotted against particle volume (note the logarithmic scale in the x axis). The minimum measured volume was 68 μm^3 while the largest was 3×10^6 μm^3. The dotted box represents the inset figure of volumetric distribution at volumes greater than 5×10^4 μm^3. To provide an idea of scale, if we were to assume a spherical shape of the Si particles, the minimum diameter would be 5 μm while the max diameter would be 180 μm. Additionally, from our images there was no indication of which particles (large or small) cracked first or cracked more. Although difficult to tell from this particular dataset, it would certainly be of interest in future work to determine any influence of particle size at the micron scale on cracking.

We also visualized the 3D nature of lithiation and the corresponding particle volume expansion via 3D renderings of the entire electrode, shown in Fig. 5, in sequential order from 0% to 100%

Fig. 4. Particle volume distribution of the entire Si electrode.

lithiation. The Si particles, colored in red (in the web version), represent a high attenuating phase while the electrode matrix was set to be invisible. In all 3D renderings, the current collector is visible at the bottom of the electrode representing a base of red, green, and blue colors. As shown in the 0% lithiation state, Si particles are located throughout the matrix in various sizes and are generally platelet-like in shape. The Si particle sizes were sieved with a 140 mesh, i.e., 105 μm maximum size, although some larger particles were able to pass through due to their anisometric geometry. The noticeable light green color surrounding some particles represents a lower attenuating phase than the Si and may result from voxel averaging of two phases at the interface. The morphology of the Si particles is similar for 25% intercalated lithium, although there is a slight change in intensity at the particle/matrix interface regions, as also shown in Fig. 3B. The green color phase now surrounds more Si particles compared to the original state and is thicker around certain particles, suggesting a density change near the particle/matrix interface, due to lithiation of the Si surface, and potentially due to the formation of SEI. After 50% lithiation, the Si particles begin to expand and the overall size of the electrode increases. A decrease in the attenuation coefficient of the Si particles is observed, and the low attenuating phase begins to penetrate the Si particles, in larger extent near the top of the electrode, which is closest to the counter electrode. This microstructural reaction is consistent with the core−shell model where Si lithiation occurs through the formation of a Li rich shell, in the form of Li_xSi, and propagation of the shell reaction front into the Si particle core. The Si particles near the top of the composite electrode experience fracture with cracks extending beyond the Li_xSi reaction front, opening additional paths for Li^+ to diffuse into the particle. At 75% lithiation, there is significant particle fracture and expansion. Finally, the electrode microstructure completely changes upon lithiation to 100%, but, as shown in Fig. 3, some Si particles still remain unlithiated.

3.2. Quantification of the evolution of individual particles

Six particles were chosen along the axis of symmetry of composite electrode (z-axis in Fig. 1) to study their temporal evolution. Here we present in detail two particles that illustrate different particle evolution as a function of lithiation; one particle is closer to and one is further from the top of the electrode. *Particle 2* was located 389 μm from the top of the electrode and *Particle 6* was located 1453 μm away. Fig. 6, shows the evolution of *Particle 2* as a function of lithiation. The leftmost figures are 2D X-ray slices through the midplane of the particle (x-y plane), the central figures display the 3D rendering of the particle based on our threshold edge detect method, and the rightmost figures display gray scale histograms of the entire cropped region of interest with an inset showing the particle histogram and the respective threshold value. The original state is shown in Fig. 6a, with the corresponding histogram showing a bimodal behavior as was shown previously in the global threshold profile in Fig. 3F for the original state of the composite electrode. The gray level threshold value determined for this state was 130 indicating any voxels with values above this number were considered as parts of a Si particle. The particle threshold profile itself consists of a distinct peak gray level of 205. After 25% lithiation, Fig. 6b, the particle appears similar to the original state, but the threshold intensity value increased to 136. Following 50% lithiation, Fig. 6c, the 3D profile of the particle begins to change as the surface appears rougher. The threshold intensity value decreases to 120 and the particle histogram begins to change profiles to a gradual peak gray level of 201. At 75% lithiation the histogram of the entire region also begins to lose its distinct bimodal nature and the Si particle visually increases in size and
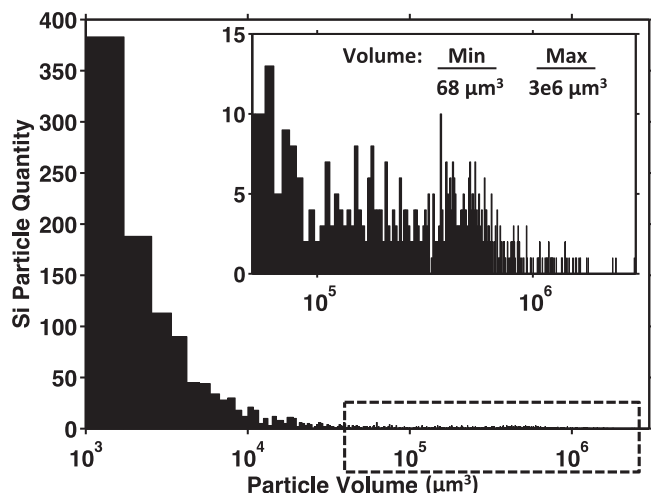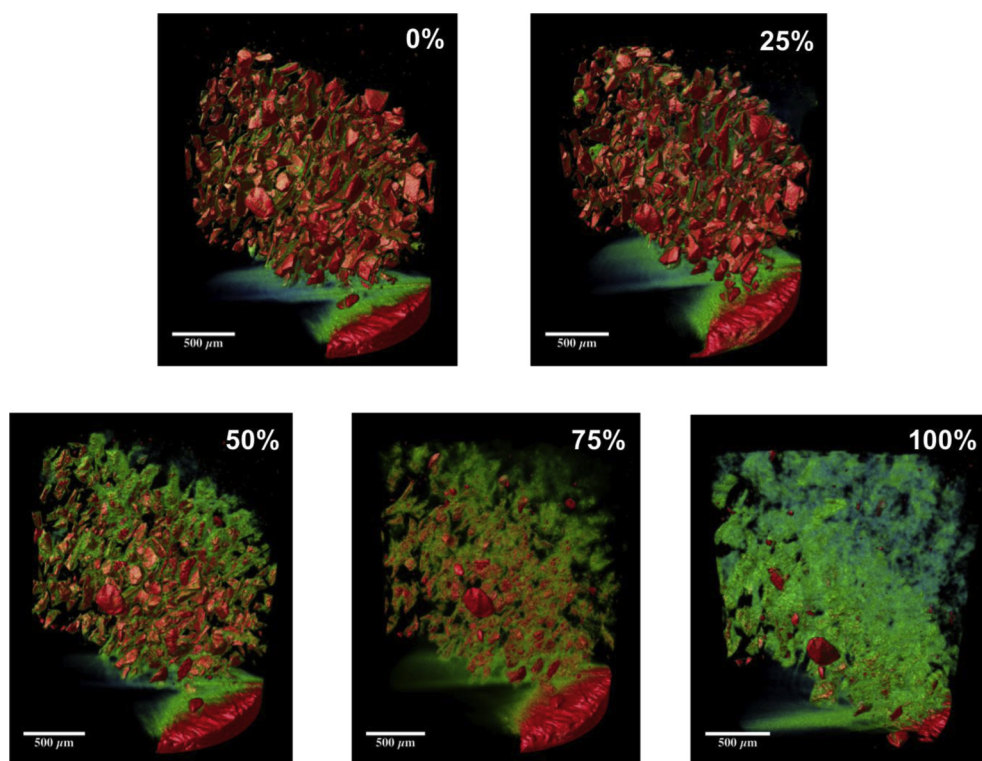
Fig. 5. 3D rendering of Si-based electrode of the LIB cell following different amounts of lithiation, 0%, 25%, 50%, 75%, and 100%. As lithiation increases, Si particles, shown in red, lose their X-ray attenuation and the low attenuating phase takes over. The low attenuating phase forming around the Si particles during 0% and 25% lithiation states represents the core–shell lithiation process. The region near the top of the 3D rendering represents the area closest to the separator. (For interpretation of the references to color in this figure legend, the reader is referred to the web version of this article.)

volume while the surface now develops cracks, Fig. 6d. At this point, the threshold edge detection method captures the outer edge of a Si particle but does not account for cracks forming within the particle. The decrease in gray scale threshold intensity between 50% and 75% lithiation demonstrates the change in density in addition to the formation of cracks within the particle (lower gray scale intensity values). The 3D profile of this Si particle shows particle dimpling in addition to shear fracture occurring at the surfaces. A gray region surrounding the particle edge is similar to the aforementioned core–shell structure, where this layer consists of alloyed Li_xSi and/or SEI. This core–shell structure is also visible in Fig. 6b and c, where a small gray region began to surround the Si particle. Following 100% intercalation (Fig. 6e) the threshold edge detection method had difficulty resolving whether a region belonged to the relevant particle or was comprised of fragments of adjacent particles. However, the volume clearly increased significantly and the particle appeared severely damaged from fracture and expansion. The global and particle histogram both shift to the left and result in a sharp peak at the left side of the gray level spectrum. Similar behavior was seen for *Particles 1* and *3* as described above for *Particle 2*.

The second particle, *Particle 6*, was the furthest from the top of the electrode at 1453 μm. In the original state, the threshold edge detection method accurately mapped out the particle edge with threshold value of 136, as shown in Fig. 7a. Following 25% lithiation (Fig. 7b), the 3D rendering of the particle showed little change. In Fig. 7c, 50% global lithiation, the beginning of particle fracture and volume expansion in all three directions are shown. The global histogram begins to lose its bimodal nature and the particle histogram gradually increases to a peak value of 200, while the threshold value for this case was 119. At 100% lithium intercalation, Fig. 7e, the threshold intensity decreased to 108, and the threshold

edge detection algorithm captured the particle edge well. Recall that in the previous case of *Particle 2*, the severity of damage in the region made it difficult to determine what belonged to the particle of interest. However, in the case of *Particle 6*, which is further away from the bulk electrolyte and counter electrode, the particle is still intact and distinguishable.

From the previous discussion, particle gray scale intensity variations were visually witnessed with increasing lithiation. In order to better determine the extent of particle transformation, the mean particle gray scale intensity as a function of lithium intercalated is shown in Fig. 8a. There is minimal intensity change between the original state and 25% lithiation. As lithiation progresses, the mean particle intensity decreases for all particles. When 75% lithiation is reached, the mean particle intensity decreases more for particles closer to the top of the electrode. After 100% lithiation, the particle intensity for *Particles 4–6* decreases further. The last three values for *Particles 1–3* were excluded after 100% lithiation because of their fully diffused nature, e.g. *Particle 2* as shown in Fig. 6e. The decrease in gray scale intensity as a function of lithiation again demonstrates the change in particle density and the formation of cracks within the particle as the edge detect method only captures the surface of the Si particle.

The overall average gray scale intensity, computed as the average of all mean particle intensity values at each lithiation step, is presented in Fig. 8b. The error bars signify the highest and lowest points of the data in Fig. 8a. The average intensity value is constant at 195 for the first lithiation step. After 25% lithiation, the average intensity decreases almost linearly supporting the conclusion of reduced attenuation coefficient of Si for increased Li intercalation. The constant average particle intensity between 0 and 25% lithiation suggests the formation of a core–shell structure during this lithiation phase.
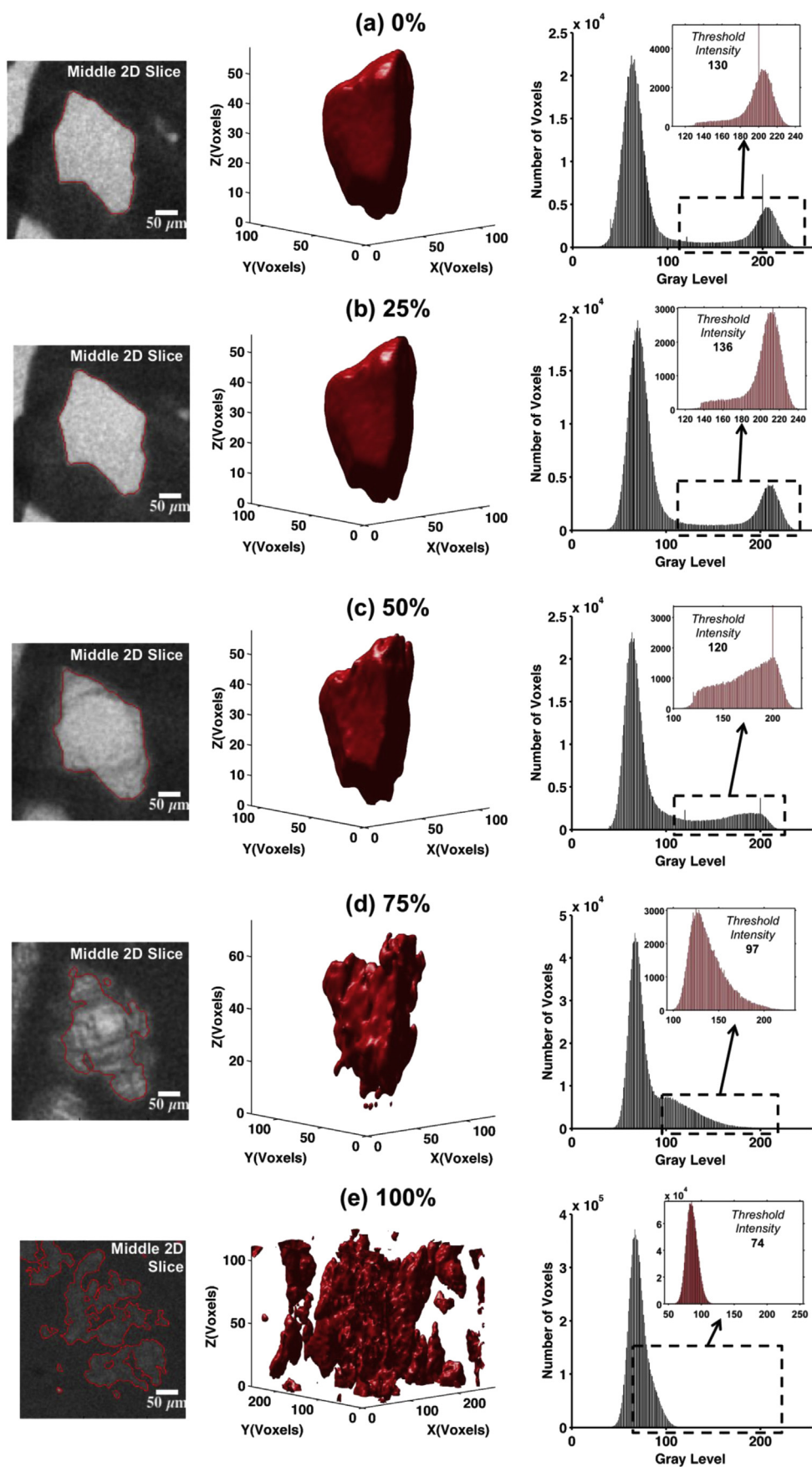
Fig. 6. Evolution of *Particle 2*, located 389 μm from the top of the electrode, at different stages of lithiation, (a) 0%, (b) 25%, (c) 50%, (d) 75%, and (e) 100% lithiation. For each lithiation step, there are three figures. The leftmost figure is the middle 2D slice (*x−y plane*) of the particle with the particle edge outline overlaid on the slice showing the result from our threshold edge detect algorithm. The central figure shows the particle in 3D where the volume shown is based on the threshold edge detect method. The rightmost figure displays the gray scale histogram of the entire cropped region of interest with an inset showing the particle histogram with the threshold value defining a particle.
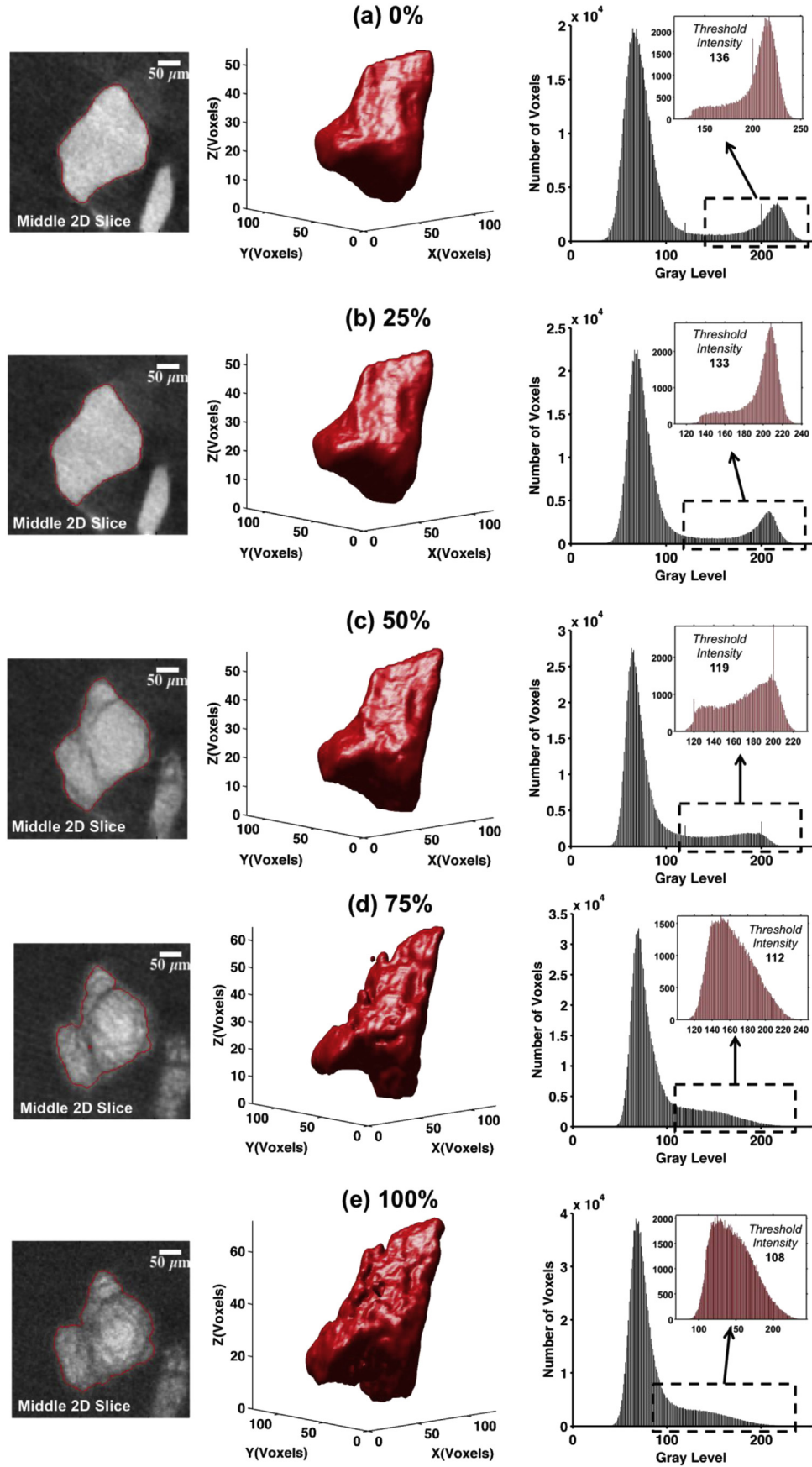
Fig. 7. Evolution of *Particle 6*, located 1453 μm from the top of the electrode, is the furthest particle selected from the top of the electrode. The particle evolution is shown at different stages of lithiation, (a) 0%, (b) 25%, (c) 50%, (d) 75%, and (e) 100% lithiation. For each lithiation step, there are three figures. The leftmost figure is the middle 2D slice (*x−y plane*) of the particle with the particle edge outline overlaid on the slice showing the result from our threshold edge detect algorithm. The central figure shows the particle in 3D where the volume shown is based on the threshold edge detect method. The rightmost figure displays the gray scale histogram of the entire cropped region of interest with an inset showing the particle histogram with the threshold value defining a particle.
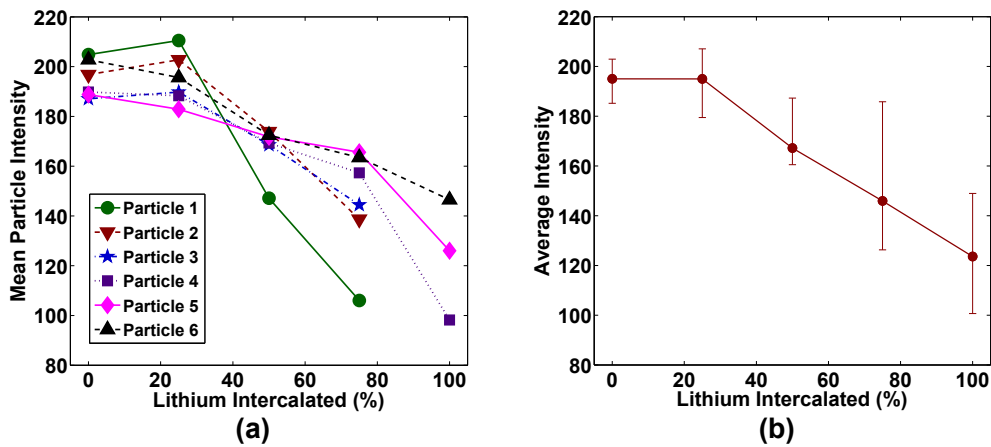
Fig. 8. (a) Mean particle intensity for *Particles 1–6* at each lithiation step based on the gray scale. The last three points for *Particles 1–3* were excluded due to indistinguishable particle fragments. (b) Averaged intensity using *Particles 1–6* at each location to yield a single value showing the trend as a function of lithiation. The error bars represent the highest and lowest values of the particle intensities considered.

Table 2
Volume expansion computed for six Si particles using threshold edge detect algorithm. The starred values mark the values in which the global histogram, used to determine the threshold value using Otsu's method, began to lose its bimodal profile.

Lithiation (%)	Particle 1	Particle 2	Particle 3	Particle 4	Particle 5	Particle 6
25	−1.7	−3.4	−1.5	0.4	−1.5	−1.8
50	41.4	4.7	5.3	4.1	0.1	13.0
75	234.8*	21.1*	47.5*	10.0*	8.7*	19.9*
100	NA	NA	NA	290.0*	108.8*	78.4*
Original volume **(10^5 μm³)**	5.49	6.57	5.04	5.46	5.09	5.23

3.3. Particle volume expansion measurements

From the 3D renderings of Si particles shown in the previous section the volume expansion was computed, Fig. 9a, as a function of distance from the top of the electrode for all six particles and for each lithiation step in. The dotted region in Fig. 9a has been blown up in

Fig. 9b showing more detail for lithiation levels of 25%–75%. The error bars represent a threshold variation of ±5 to account for any error in determining the threshold value using Otsu's method [15]. For the filled circle data points, 25% lithiation, essentially no volume expansion is observed. Following 50% lithiation, diamond data points, the volume increases for all particles but *Particle 1* and *Particle 6* experience the most increase at 41% and 13%, respectively. This is expected, since the electrolyte concentration is higher at the top and bottom of the electrode rather than the center of the containing tube. After 75% lithiation, triangle data points, volume expansion increases further where *Particle 1* and *Particle 3* experience the highest volume expansion at 235% and ~48%, respectively. *Particle 1* is expected to experience the largest volume expansion due to its proximity to the top of the electrode. *Particle 3* is the smallest particle analyzed and should lithiate faster than the others [5]. After 100% lithiation, square data points, the volume expansion increases by an order of magnitude for *Particles 4–6*. The data points for *Particles 1–3* were excluded in this measurement because of the severity of particle fracture as mentioned in the previous section. The maximum computed volume expansion was for *Particle 4* reaching up to 290%.
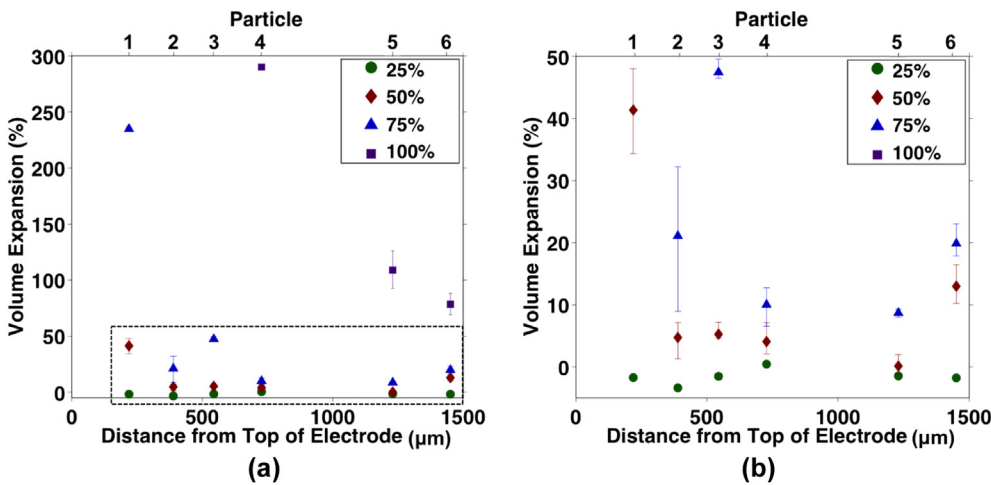

Fig. 9. Volume expansion measurements for *Particles 1–6*, selected throughout the Si-based electrode, as a function of distance from the top of the electrode for each lithiation step. The left figure (a) shows volume expansion measurements up to 290% after 100% lithiation. The dotted box at the lower part of the plot is the location of the figure on the right (b), which is a close up of the first three lithiation steps. The error bars represent a threshold variation of ±5 to account for any error in determining the threshold value using Otsu's method.

Table 2 summarizes the calculated volume expansion for Si *Particles 1—6*. The asterisks next to numbers for 75% and 100% lithiation represent values in which the bimodal profile from the global histogram begins to fade. Additionally, the initial volume (μm^3) of each particle is shown to provide a reference for the particle size. Notably, there is a discrepancy in the results for *Particle 2* and *Particle 3*. Although *Particle 2* was closer to the top of the electrode, which should result in a faster diffusion in comparison to *Particle 3*, the volume expansion for *Particle 3* was more significant than *Particle 2* suggesting that smaller particles can expand disproportionally compared to larger ones, contrary to the discussion in Ref. [5]. However, several factors influence the lithiation rate in a 3D locally electrically heterogeneous matrix in addition to the matrix porosity and the particle-matrix electrical contact.

4. Conclusions

The microstructural evolution of a Si-based composite electrode is not well understood and this paper presents a first detailed account of the 3D evolution of a Si-based composite anode in a LIB cell. The global 3D microstructure was quantified at different stages of lithiation during the first half cycle with attendant volume expansion and fracture of Si particles. More specifically, the main conclusions and contributions from this work are the following:

1) Si particle volumetric expansion measurements using a novel threshold edge detection method provide values for Si expansion as high as 290% at 100% lithiation, generally, with decreasing volume expansion at distances away from the top of the electrode.
2) Crack initiation of micron scale Si particles during lithiation occurs on the external surface with inward propagation.
3) The global and particle intensity histograms correlated decreasing X-ray attenuation with increasing lithiation yielding particle density changes due to a combination of the Li rich shell penetrating the Si core and SEI formation.
4) Less than 5% of the total Si particles in the electrode never experience lithiation, or complete lithiation, potentially due to particle-matrix electrical contact loss, porosity, etc.
5) Finally, smaller particles can expand more in relative volume and faster than larger ones.

References

[1] M. Asao, S. Kawakami, T. Ogura, Electrode material for lithium secondary battery, electrode structure comprising the electrode material and secondary battery comprising the electrode structure, Google Patents, 2008.
[2] L.Y. Beaulieu, K.W. Eberman, R.L. Turner, L.J. Krause, J.R. Dahn, Electrochem. Solid-State Lett. 4 (9) (2001) A137.
[3] T. Bryant, A. Waldman, Applied Radiological Anatomy for Medical Students, Introduction to Technology of Imaging Cambridge University Press, 2007.
[4] C.K. Chan, H. Peng, G. Liu, K. McIlwrath, X.F. Zhang, R.A. Huggins, Y. Cui, Nat. Nanotechnol. 3 (1) (2008) 31—35.
[5] S.-C. Chao, Y.-C. Yen, Y.-F. Song, Y.-M. Chen, H.-C. Wu, N.-L. Wu, Electrochem. Commun. 12 (2) (2010) 234—237.
[6] Y.-T. Cheng, M.W. Verbrugge, J. Electrochem. Soc. 157 (4) (2010) A508.
[7] R. Deshpande, Y.-T. Cheng, M.W. Verbrugge, A. Timmons, J. Electrochem. Soc. 158 (6) (2011) A718.
[8] M. Ebner, F. Geldmacher, F. Marone, M. Stampanoni, V. Wood, Adv. Energy Mater. 3 (7) (2013) 845—850.
[9] M. Ebner, F. Marone, M. Stampanoni, V. Wood, Science 342 (6159) (2013) 716—720.
[10] U. Kasavajjula, C. Wang, J. Appleby, J. Power Sources 163 (2) (2007) 1003—1039.
[11] D. Kehrwald, P.R. Shearing, N.P. Brandon, P.K. Sinha, S.J. Harris, J. Electrochem. Soc. 158 (12) (2011) A1393.
[12] I. Kovalenko, B. Zdyrko, A. Magasinski, B. Hertzberg, Z. Milicev, R. Burtovyy, I. Luzinov, G. Yushin, Science 334 (6052) (2011) 75—79.
[13] A. Magasinski, P. Dixon, B. Hertzberg, A. Kvit, J. Ayala, G. Yushin, Nat. Mater. 9 (4) (2010) 353—358.
[14] M.N. Obrovac, L.J. Krause, J. Electrochem. Soc. 154 (2) (2007) A103.
[15] N. Otsu, IEEE Trans. Syst. Man. Cybern. SMC 9 (1) (1979) 62—66.
[16] B. Scrosati, J. Garche, J. Power Sources 195 (9) (2010) 2419—2430.
[17] P.R. Shearing, N.P. Brandon, J. Gelb, R. Bradley, P.J. Withers, A.J. Marquis, S. Cooper, S.J. Harris, J. Electrochem. Soc. 159 (7) (2012) A1023—A1027.
[18] P.R. Shearing, L.E. Howard, P.S. Jergensen, N.P. Brandon, S.J. Harris, Electrochem. Commun. 12 (3) (2010) 374—377.
[19] J. Tarascon, M. Armand, Nature 414 (2001) 359—367.
[20] F. Tariq, V. Yufit, M. Kishimoto, P.R. Shearing, S. Menkin, D. Golodnitsky, J. Gelb, E. Peled, N.P. Brandon, J. Power Sources 248 (2014) 1014—1020.
[21] C. Wang, H. Wu, Z. Chen, M.T. McDowell, Y. Cui, Z. Bao, Nat. Chem. 5 (12) (2013) 1042—1048.
[22] J.R. Wilson, J.S. Cronin, S.A. Barnett, S.J. Harris, J. Power Sources 196 (7) (2011) 3443—3447.
[23] M. Winter, J. Besenhard, Electrochim. Acta 45 (1999) 31—50.
[24] N. Yoshizawa, O. Tanaike, H. Hatori, K. Yoshikawa, A. Kondo, T. Abe, Carbon 44 (12) (2006) 2558—2564.
[25] V. Yufit, P. Shearing, R.W. Hamilton, P.D. Lee, M. Wu, N.P. Brandon, Electrochem. Commun. 13 (6) (2011) 608—610.
[26] K. Zhao, M. Pharr, S. Cai, J.J. Vlassak, Z. Suo, J. Am. Ceram. Soc. 94 (2011) s226—s235.
[27] K. Zhao, M. Pharr, Q. Wan, W.L. Wang, E. Kaxiras, J.J. Vlassak, Z. Suo, J. Electrochem. Soc. 159 (3) (2012) A238—A243.